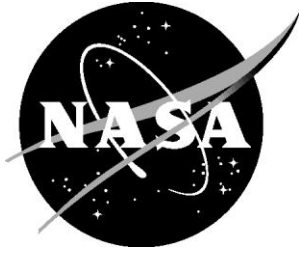


NASA/TM-20240006013



# Transitional Flow in the Wake of a Pseudorandom Roughness on a Supersonic Flat Plate

*Amanda Chou, Andrew N. Leidy, Michael A. Kegerise, and Rudolph A. King  
Langley Research Center, Hampton, Virginia*

---

June 2024

## NASA STI Program Report Series

Since its founding, NASA has been dedicated to the advancement of aeronautics and space science. The NASA scientific and technical information (STI) program plays a key part in helping NASA maintain this important role.

The NASA STI program operates under the auspices of the Agency Chief Information Officer. It collects, organizes, provides for archiving, and disseminates NASA's STI. The NASA STI program provides access to the NTRS Registered and its public interface, the NASA Technical Reports Server, thus providing one of the largest collections of aeronautical and space science STI in the world. Results are published in both non-NASA channels and by NASA in the NASA STI Report Series, which includes the following report types:

- **TECHNICAL PUBLICATION.** Reports of completed research or a major significant phase of research that present the results of NASA Programs and include extensive data or theoretical analysis. Includes compilations of significant scientific and technical data and information deemed to be of continuing reference value. NASA counterpart of peer-reviewed formal professional papers but has less stringent limitations on manuscript length and extent of graphic presentations.
- **TECHNICAL MEMORANDUM.** Scientific and technical findings that are preliminary or of specialized interest, e.g., quick release reports, working papers, and bibliographies that contain minimal annotation. Does not contain extensive analysis.
- **CONTRACTOR REPORT.** Scientific and technical findings by NASA-sponsored contractors and grantees.

- **CONFERENCE PUBLICATION.** Collected papers from scientific and technical conferences, symposia, seminars, or other meetings sponsored or co-sponsored by NASA.
- **SPECIAL PUBLICATION.** Scientific, technical, or historical information from NASA programs, projects, and missions, often concerned with subjects having substantial public interest.
- **TECHNICAL TRANSLATION.** English-language translations of foreign scientific and technical material pertinent to NASA's mission.

Specialized services also include organizing and publishing research results, distributing specialized research announcements and feeds, providing information desk and personal search support, and enabling data exchange services.

For more information about the NASA STI program, see the following:

- Access the NASA STI program home page at <http://www.sti.nasa.gov>
- Help desk contact information: <https://www.sti.nasa.gov/sti-contact-form/> and select the "General" help request type.

NASA/TM-20240006013



# Transitional Flow in the Wake of a Pseudorandom Roughness on a Supersonic Flat Plate

*Amanda Chou, Andrew N. Leidy, Michael A. Kegerise, and Rudolph A. King  
Langley Research Center, Hampton, Virginia*

National Aeronautics and  
Space Administration

Langley Research Center  
Hampton, Virginia 23681-2199

June 2024

The use of trademarks or names of manufacturers in this report is for accurate reporting and does not constitute an official endorsement, either expressed or implied, of such products or manufacturers by the National Aeronautics and Space Administration.

Available from:

NASA STI Program / Mail Stop 050  
NASA Langley Research Center  
Hampton, VA 23681-2199

# Transitional Flow in the Wake of a Pseudorandom Roughness on a Supersonic Flat Plate

Amanda Chou\*, Andrew N. Leidy†, Michael A. Kegerise‡, and Rudolph A. King‡  
NASA Langley Research Center, Hampton, VA, 23681, USA

A roughness patch defined by a two-dimensional series of sine waves was installed in a highly-polished flat plate model immersed in a supersonic quiet flow. The NASA Langley Research Center Supersonic Low Disturbance Tunnel is capable of providing a Mach 3.5 flow with low freestream acoustic noise and low turbulence levels. Measurements made with a hot-wire probe downstream of the roughness patch showed the presence of two instability modes centered near 75 kHz that caused transition in the measurement region at a freestream unit Reynolds number of  $Re = 12.6 \times 10^6/m$ . This result differed from previous measurements with the roughness patch rotated  $180^\circ$  from the current configuration. Previous measurements showed the development of a single instability near 100 kHz in the wake of the tallest roughness in the roughness patch that did not transition at the same Reynolds number.

## I. Nomenclature

$A_{nm}$	=	Fourier mode amplitude
$G_{xx}$	=	wavelength spectra of the pseudorandom pattern
$h$	=	roughness height, $\mu\text{m}$
$h_w$	=	nominal analytic definition of roughness height, $\mu\text{m}$
$h_{taper}$	=	taper function of roughness height
$P_{11}$	=	power spectral density of signal from wire 1
$P_{22}$	=	power spectral density of signal from wire 2
$P_{12}$	=	cross-spectral density of signals from wires 1 and 2
Rot1	=	initial rotation of pseudorandom roughness insert
Rot2	=	current rotation of pseudorandom roughness insert ( $180^\circ$ from Rot1)
$x$	=	streamwise coordinate on the flat plate, mm
$y$	=	wall-normal coordinate on the flat plate, mm
$z$	=	spanwise coordinate on the flat plate, mm
$x_T$	=	streamwise tunnel coordinate measured from the throat, mm
$y_T$	=	vertical tunnel coordinate measured from the throat, mm
$z_T$	=	spanwise horizontal coordinate measured from the throat, mm
$\gamma^2$	=	magnitude-squared coherence of a signal
$\eta$	=	nondimensional Blasius boundary layer distance
$\lambda$	=	wavelength of pseudorandom pattern in the streamwise direction, mm
$\phi_{nm}$	=	Fourier mode phase
$\rho u$	=	mass flux, $\text{kg}\cdot\text{m}^2/\text{s}$
$(\cdot)_e$	=	edge value
$\langle \cdot \rangle$	=	RMS amplitude

## II. Introduction

Prediction of roughness-induced transition is a practical requirement for the optimized design of high-speed vehicles, which rely on a reduction of thermal stresses and drag for higher performance. This reduction is affected by boundary

---

\*Research Aerospace Engineer, Flow Physics & Control Branch, M/S 170, and AIAA Associate Fellow.

†Research Aerospace Engineer, Flow Physics & Control Branch, M/S 170, and AIAA Member

‡Research Aerospace Engineer, Flow Physics & Control Branch, M/S 170

layer transition, which may be caused by unavoidable roughness such as inherent surface material roughness and deterioration or roughness in the form of sensing elements, fasteners, etc. A better understanding of transition resulting from roughness can help inform acceptable manufacturing tolerances or maintenance requirements on operational flight vehicles.

Over the past 12 years, an effort targeted at understanding the prediction and growth of instabilities in the wake of roughness has been ongoing within the Revolutionary Computational Aerosciences discipline under the NASA Transformational Tools and Technologies Project. The work first started with preliminary design of an experiment, reported in Ref. [1], where an appropriate freestream condition and roughness height were found for the study. Subsequently, several different planforms for a fixed roughness height were investigated in Ref. [2]. These were the first combination of measurements and stability analysis that were made in a supersonic boundary layer that showed the growth of a wake instability could be predicted using two-dimensional spatial stability analysis. Direct numerical simulation studies [3] also showed that the shape of the instability modes in the wake of isolated roughness could be affected by the angle of incidence of three-dimensional planar waves. Next, tandem roughness elements of different planforms were used to show the effect on instability growth of the interaction of multiple elements placed in a streamwise array [4–6]. These results showed that adding elements could either delay or promote transition and change the dominant instability in the wake.

More recently, an analytic function was used to define multiple elements in both a streamwise and spanwise array by defining a sinusoidal surface known as an egg crate roughness [7, 8]. This analytic definition allows for a smooth surface to be specified in computational codes while also providing a relevant physical shape. In this study, transition was found to be delayed in comparison to the wakes of isolated roughness elements and was more accurately predicted when the incoming instabilities to the roughness patch were considered as part of the growth of the instabilities downstream.

The experimental extension of this work on a supersonic flat plate into a pseudorandom roughness defined by an analytic function was first presented in [9]. This pseudorandom roughness was inspired by previous low-speed studies by an experimental group at Texas A & M University and a computational group at University of Texas, who have conducted numerous studies of a similar roughness patch [10–14]. The development of the pseudorandom roughness in the present experiments uses the same methodology as these low-speed experiments of randomizing amplitude and phase in a series of sine waves. The low-speed studies yielded several discoveries for pseudorandom roughness: that the tallest elements of pseudorandom roughness patches can cancel out disturbances from each other [12, 13] and that the effect of the tallest roughness in a distributed roughness is diminished by the presence of distributed roughness [11, 14]. This paper will explore differences observed on a supersonic flat plate when the pseudorandom roughness was rotated 180° compared to earlier measurements from the first orientation in Ref. [9].

### III. The Supersonic Low Disturbance Tunnel

Measurements were made in the NASA Langley Research Center Supersonic Low Disturbance Tunnel (SLDT) to characterize the freestream disturbance environment. Freestream measurements of the facility along the centerline of the tunnel were made prior to and after testing the flat plate in the tunnel and show almost no variation from reports in the previous years, dating back to the 1980s [15, 16]. These measurements were made with both a dual hot wire as well as a pitot tube with a screenless flush-mounted Kulite pressure transducer at the tip.

The SLDT is the first quiet tunnel that was built in the United States in the late 1970s [15]. A highly-polished Mach 3.5 two-dimensional rapid-expansion nozzle was used for the measurements presented in this paper. Suction slots at the throat are present to allow a fresh boundary layer to grow along the length of the nozzle. Along with the mirror finish of the nozzle, these suction slots serve to maintain laminar flow on the nozzle walls. During these experiments, the facility operational run time was sufficiently long that the flat plate model has reached an equilibrium temperature, with the leading edge near an adiabatic wall temperature. Conditions were held relatively constant at a total pressure of  $241.7 \pm 0.6$  kPa and a total temperature of approximately  $319.2 \pm 0.2$  K for a freestream unit Reynolds number of  $12.6 \times 10^6/\text{m}$ .

A constant-temperature anemometer with a symmetric bridge was used for the freestream hot-wire measurements and the two wires at the tip of the probe were operated at the same high overheat ratio to be sensitive to mass flux. The lengths of both hot wires were on the order of 1 mm and the diameters were 5  $\mu\text{m}$  (Fig. 1). The tuning of both hot wires was matched as closely as possible to have a frequency response of approximately 160 kHz. The hot-wire measurements were sampled at 500 kHz for 2 s. An 8-pole low-pass anti-aliasing filter was applied to these measurements at 200 kHz and a 4-pole high-pass filter was applied at 100 Hz to reduce any contributions from electronic line noise.

This experiment was conducted at a freestream unit Reynolds number of  $12.6 \times 10^6/\text{m}$ , the same condition as the

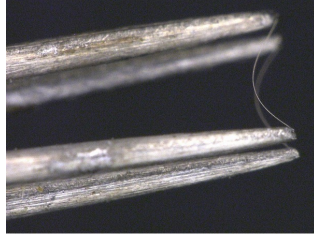


**Fig. 1** Picture of dual hot wire tip on a freestream probe under 100x magnification. Wires are 5  $\mu\text{m}$  in diameter, greater than 1 mm long, and approximately 0.25 mm apart. [Credit: NASA]

previous measurements in the wake of the egg crate roughness [8] and the original pseudorandom roughness [9]. Power spectral densities (PSDs) of the freestream mass-flux fluctuations were estimated using Welch’s method with 5000-point Hann windows and 50% overlap. The coherence of the two wires was also estimated using Welch’s method such that:

$$\gamma^2 = \frac{|P_{12}|^2}{P_{11}P_{22}} \quad (1)$$

where  $\gamma^2$  is the magnitude-squared coherence,  $P_{12}$  is the cross-spectral density of the two wires, and  $P_{11}$  and  $P_{22}$  are the power-spectral densities of the first and second wires, respectively. A coherent power spectra was determined by  $\gamma^2 P_{11}$  or  $\gamma^2 P_{22}$ , to mitigate the effects of the contribution of electronic noise to the measurements. Root-mean-square values of the mass-flux fluctuations in the freestream were computed by integrating the coherent power spectral densities between 100 Hz and 100 kHz and taking the square root. The measurements of the mass flux were under 0.1% in the quiet core of the facility, where measurements were made on the flat plate model. These freestream measurements are displayed as contour plots in Fig. 2, where the nozzle and model contours are supplied for reference. The uniform flow region begins at approximately  $x_T = 127$  mm and the quiet core ends at approximately  $x_T = 389$  mm from the nozzle throat along the nozzle centerline. These locations correspond to the coordinate system on the flat plate of  $x = -12.7$  to 228 mm. For clarity, the measurement region is provided in Fig. 2b as a dotted white line.

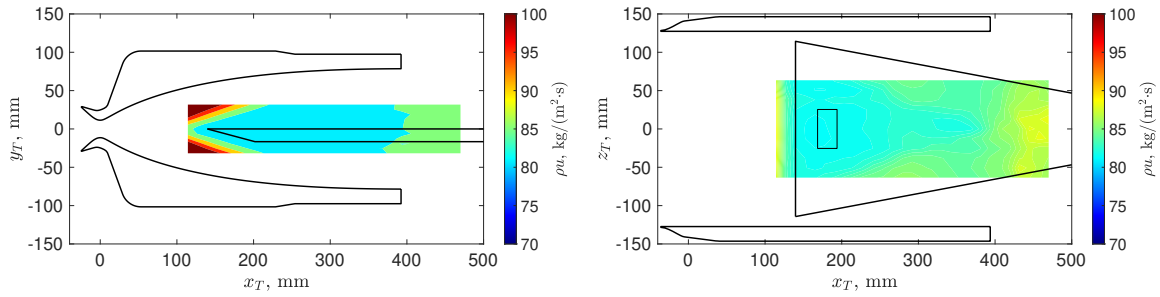
Mean and fluctuating pitot pressure were also measured with an absolute-pressure Kulite transducer that was flush-mounted to the tip of a pitot tube with a 2.26-mm (0.089-inch) outer diameter. The Kulite transducer had no screen and RTV filler around the sensing element. The pressure measurements were sampled at 500 kHz for 2 s. An 8-pole low-pass anti-aliasing filter was applied to these measurements at 200 kHz and a 4-pole high-pass filter was applied at 100 Hz to reduce any contributions from electronic line noise. Similar to the mass-flux measurements, the pressure measurements in Fig. 3 show fairly uniform Mach number and acoustic disturbance environment across the measurement region.

## IV. The Flat Plate Model and Roughness Insert

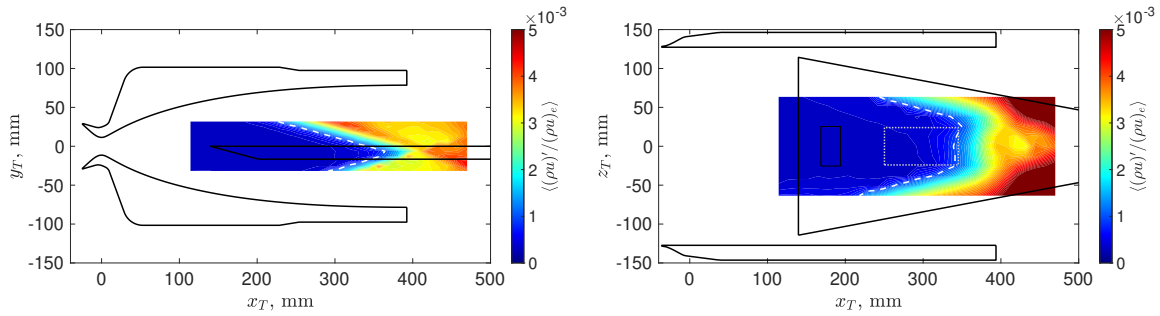
### A. The Flat Plate Model

A stainless steel flat plate model was made with a blind pocket to house an insert for different distributed roughness geometries. Figure 4 shows the model with an egg crate roughness installed. The surface finish of the flat plate model was specified to be a 0.05- $\mu\text{m}$  (2- $\mu\text{in.}$ ) root-mean-square finish. The leading-edge thickness varies between 76–127  $\mu\text{m}$ , as measured under a microscope using a silicone rubber mold of the leading edge.

The pocket for the roughness inserts is located 28.8 mm from the leading edge of the flat plate and centered in the  $z$ -direction along the same centerline as the flat plate. The center of the roughness inserts is  $x = 41.5$  mm from the leading edge of the flat plate, which is identical to the position of the isolated roughness elements that were tested in Ref. [2] and the position of the farthest upstream roughness elements in Ref. [6]. This location for the roughness insert is meant to coincide with the neutral point of the dominant first-mode instability wave that grows on the flat plate at the Mach number and Reynolds number in these references. Results from a distributed periodic roughness pattern such as an egg crate roughness [8] indicate that the roughness affects any incoming first-mode instability waves in order to produce instabilities downstream.

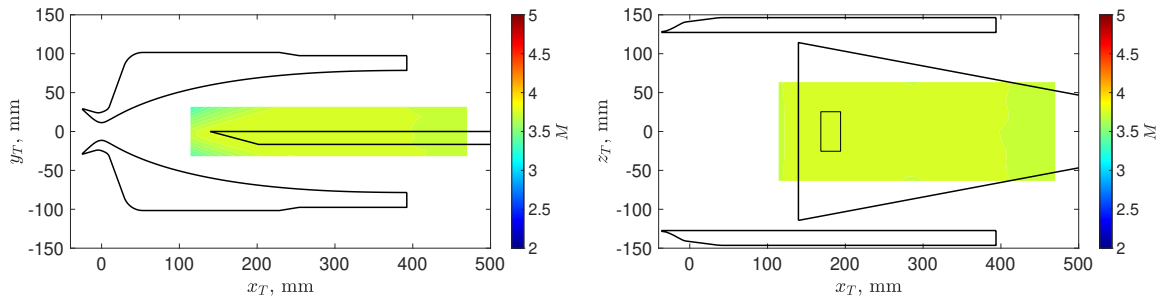


(a) Mass-flux measurements along the center planes (left) in plane with contoured nozzle and (right) in plane with flat side walls.

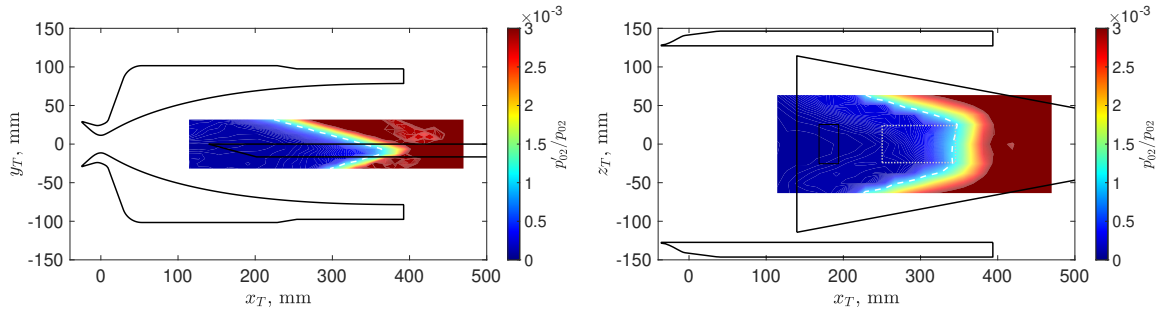


(b) Mass-flux fluctuation measurements along the center planes (left) in line with contoured nozzle and (right) in line with flat side walls.

**Fig. 2** Mass flux and mass-flux fluctuation contours in an empty tunnel:  $M_\infty = 3.5$ ,  $Re = 12.6 \times 10^6/\text{m}$ . White dashed lines are the limit of a 0.1% mass-flux fluctuation. Black solid lines are the hard boundaries of the nozzle, flat plate, and roughness insert. White dotted lines in Fig. 2b(right) are the measurement region.



(a) Mach number contours along the center planes (left) in plane with contoured nozzle and (right) in plane with flat side walls.



(b) Pitot pressure fluctuation measurements along the center planes (left) in line with contoured nozzle and (right) in line with flat side walls.

**Fig. 3** Mach number and pitot pressure fluctuation contours in an empty tunnel:  $M = 3.5$ ,  $Re = 12.6 \times 10^6/m$ . White dashed lines are the limit of a 0.1% pitot pressure fluctuation. Black solid lines are the hard boundaries of the nozzle, the flat plate, and roughness insert. White dotted lines in Fig. 3b(right) are the measurement region.



**Fig. 4 Flat plate model with coordinate system in red. [Credit: NASA]**

### B. Pseudorandom Roughness Insert

The pseudorandom roughness height ( $h_w$ ) is defined by a two-dimensional Fourier series of the form:

$$h_w = \sum_{n=-N}^N \sum_{m=-M}^M A_{nm} \cos \left( \frac{2\pi n(x - x_0)}{\lambda_x} + \frac{2\pi m z}{\lambda_z} + \phi_{nm} \right) \quad (2)$$

where  $N$  and  $M$  are the number of modes in the  $x$ - and  $z$ -direction, respectively,  $A_{nm}$  is a random amplitude,  $\phi_{nm}$  is a random phase,  $x_0$  is the streamwise centerline of the roughness patch, and  $\lambda_x$  and  $\lambda_z$  are the wavelength of the repeated roughness patch in the  $x$ - and  $z$ -direction, respectively. With  $\lambda_x$  set so that  $\lambda_x = \frac{1}{2}\lambda_z$ , the roughness pattern does not repeat in the streamwise direction and repeats once in the spanwise direction. Random coefficients of  $A_{nm}$  and  $\phi_{nm}$  with uniform distribution are saved to later define the boundary conditions. A tapering function is used to transition the roughness to the smooth surface of the flat plate insert so that  $h = h_w h_{taper}$  and  $h_{taper}$  is given by

$$h_{taper} = \begin{cases} \frac{1}{2} \left( 1 + \frac{2}{\sqrt{\pi}} \int_0^{x-x_0-x_{taper}} e^{-t^2} dt \right) & \text{if } x - x_0 \leq L_x/2, \\ \frac{1}{2} \left( 1 + \frac{2}{\sqrt{\pi}} \int_0^{L_x-x_{taper}-x} e^{-t^2} dt \right) & \text{if } x - x_0 \geq L_x/2, \\ \frac{1}{2} \left( 1 + \frac{2}{\sqrt{\pi}} \int_0^{z+L_z/2-x_{taper}} e^{-t^2} dt \right) & \text{if } z \leq 0, \\ \frac{1}{2} \left( 1 + \frac{2}{\sqrt{\pi}} \int_0^{L_z/2-x_{taper}-z} e^{-t^2} dt \right) & \text{if } z \geq 0, \\ 1 & \text{otherwise,} \end{cases} \quad (3)$$

where  $x_{taper}$  is the tapering length of 1.588 mm,  $L_x = 25.4$  mm is the streamwise dimension of the insert, and  $L_z = 50.8$  mm is the spanwise dimension of the insert. The idealized analytic function of the pseudorandom roughness is provided in Fig. 5 relative to the local boundary layer thickness over the roughness pattern. The vertical axis of Fig. 5 shows the streamwise location of the insert on the flat plate, and the horizontal axis of the figure shows the spanwise coordinate of the flat plate.

Measurements of the as-built pseudorandom roughness insert for the flat plate were made with a three-dimensional one-shot macroscope and are provided in Fig. 6a. Measurement dropout regions are shown in dark blue. The tallest protuberances are approximately +273  $\mu\text{m}$  and the deepest cavities are -272  $\mu\text{m}$  in height relative to the model surface, although the surrounding local maxima and minima are similar in height.

Measurements of steps created by any nonuniformity of the insert were made with a contact profilometer with a tip radius of 2  $\mu\text{m}$ . The pseudorandom roughness insert did not fit as well in the pocket in the flat plate when rotated from its original position described in Ref. [9], producing as much as an 8  $\mu\text{m}$  step near the upstream  $-z$  corner of the insert and the downstream  $+z$  corner of the insert. A mold of the insert was also made with a two-part silicone rubber compound to capture a three-dimensional replica of the overall fit of the insert and scanned with the same one-shot macroscope as

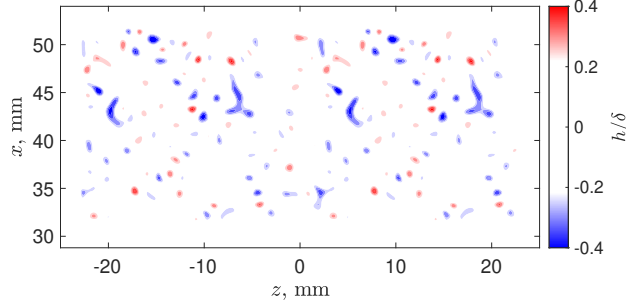


**Fig. 5** Roughness heights in the idealized pseudorandom roughness insert relative to the local boundary layer thickness.

previously mentioned. The inverted measurements of the silicone rubber mold of the installed roughness is provided in Fig. 6b. Some distortion is noted around the edges of the mold, due to the pliable nature of the silicone rubber and how it was removed from the surface of the flat plate. This distortion is not representative of the surface of the flat plate.

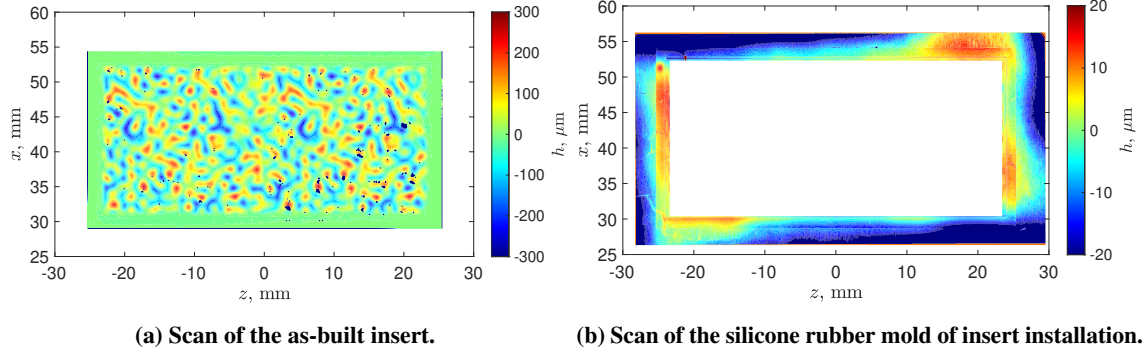


**Fig. 6** The as-built pseudorandom roughness insert and silicone rubber mold of the edges of the as-installed pseudorandom roughness insert on the flat plate.

## V. Hot-Wire Anemometry Measurements

Measurements of the wake of the pseudorandom roughness were made with a constant temperature anemometer with a symmetric bridge. The platinum-coated tungsten sensing element used for boundary layer measurements was approximately 0.5 mm in length and 3.8  $\mu\text{m}$  in diameter. These wires are mounted to the tip of a probe that has been designed to produce as little flow disturbance as possible (Fig. 7). Note that this is a different probe and wire than used for the freestream measurements. Reynolds-averaged Navier-Stokes simulations indicate that the maximum flow disturbance produced by these probes yields a 2% change in mass flux. These hot wires were operated at a high overheat ratio in order to be more sensitive to mass flux, and a temperature correction was used to calibrate these sensors, as in Ref. [1]. Measurements were sampled at a rate of 1 MHz for 1 second at each  $(x, y, z)$ -station.

## VI. Measurements of the Mean Mass Flux

Measurements were made at several streamwise stations downstream of the rotated pseudorandom roughness. The mean mass flux across the span of the flat plate is provided in Fig. 8. Flow features are repeated once across the span, as expected, given that the pseudorandom roughness pattern also repeats across the span. This effect has been observed in previous work described in Ref. [9].

The measurements were conducted over multiple runs, sometimes spanning a couple days. Some evidence of the effects on the measurements are notable in a difference of approximately  $\pm 6\%$  seen near the edge of the boundary layer for different portions of the measurements across the span. For example, in Fig. 8a, there is a set of vertical bands that

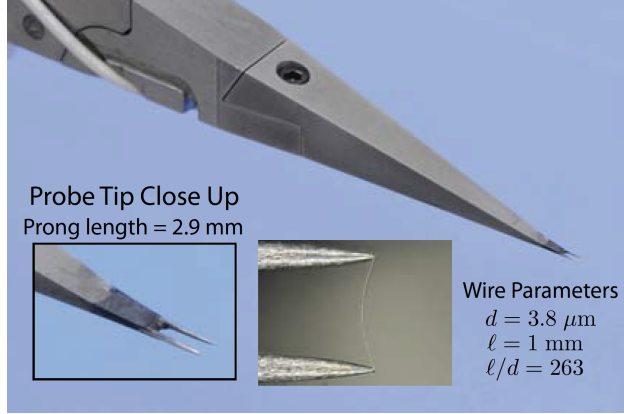


**Fig. 7 Closeup picture of a hot wire probe used for boundary layer measurements. [Credit: NASA]**

vary in shades of red between  $z = -3.6$  and  $-3.2$  mm and  $z = +3.2$  and  $+3.6$  mm. This is due to a slight difference in freestream Reynolds number for the data taken between  $z = -3.6$  and  $+3.6$  mm on one run and the runs at  $z > +3.2$  mm or  $z < -3.2$  mm. The banded colors on the contour maps occurs when interpolating points taken between the two sets of data, as there is some overlap between the two data sets.

To quantify the changes in mean flow distortion, a modified version of the streak strength defined by Fransson et al. [17] is used:

$$A_{\rho u} = \frac{1}{2} \left( \rho u (y)_{\text{high}} - \rho u (y)_{\text{low}} \right) \quad (4)$$

where  $\rho u (y)_{\text{high}}$  is the mean mass flux profile in a high mass-flux streak and  $\rho u (y)_{\text{low}}$  is the mean mass flux profile in a low mass-flux streak. The streak amplitude can also be defined as the wall-normal maximum of the streak strength profile. Streak strength profiles were not made for these data at each  $x$ -location, due to the limited spanwise extent of some of the measurements. Streak strength profiles have been useful in helping to quantify distortion in the wake of a single roughness element or in a spanwise-periodic roughness distribution. For a pseudorandom or any other distributed roughness, this measure of distortion may not indicate local transition events. Therefore, further information supporting whether the flow has transitioned will be shown in the next section discussing the fluctuating mass-flux measurements.

For locations of  $x = 110.6$  mm,  $179.7$  mm, and  $205.6$  mm, the streak strength profiles are given in Fig. 9, plotted against the nondimensional Blasius boundary layer parameter  $\eta$ . The mean flow distortion is relatively consistent down the length of the plate at these three stations. The streak strength profiles show that the mean flow distortion changes only slightly between  $x = 110.6$  mm (Fig. 8a) and the farthest downstream station of  $x = 205.6$  mm (Fig. 8f). The minor differences in streak strength profiles between  $x = 179.7$  mm (Fig. 8d) and  $x = 205.6$  mm (Fig. 8f) indicate almost no change in mean flow distortion across the span.

## VII. Measurements of the Fluctuating Mass Flux

Power spectra of each of the hot-wire measurements were made using Welch's method of spectrum estimation, using Hann windows of at least 2048 points and 50% overlap. This method produces a frequency resolution of 488 Hz in the power spectra. The root-mean-square (RMS) quantities of the mass-flux fluctuations were computed by integrating the power spectra across a 5-kHz bandwidth centered at several frequencies, and then taking the square root of this value. The maximum RMS mass-flux fluctuation amplitudes were found for these different bands, and the contours of RMS mass-flux fluctuation are given for the most-amplified frequency in the power spectra in Fig. 10. This frequency is approximately 75 kHz, but the highest amplitude disturbance can be as low as 72.7 kHz at the farthest upstream station or up to 79.1 kHz at the farthest downstream station.

The largest-amplitude instability was observed near the centerline of the plate, between  $z = -5$  and  $-3$  mm in Fig. 10. This instability is clearly repeated between  $z = +21$  mm and  $+24$  mm at  $x = 110.6$  mm (Fig. 10a). However, these locations were not expected to produce the largest disturbances, as there is no discernible roughness that is higher amplitude than the surrounding roughness shown in Fig. 6a to prompt the instability growth. The largest amplitude surface roughness near the centerline is now located closer to  $z = 7.75$  mm, yet no instabilities appear in that region. There is a remote possibility that this inconsistency may be due to a misalignment in the probe traverse and the flat plate

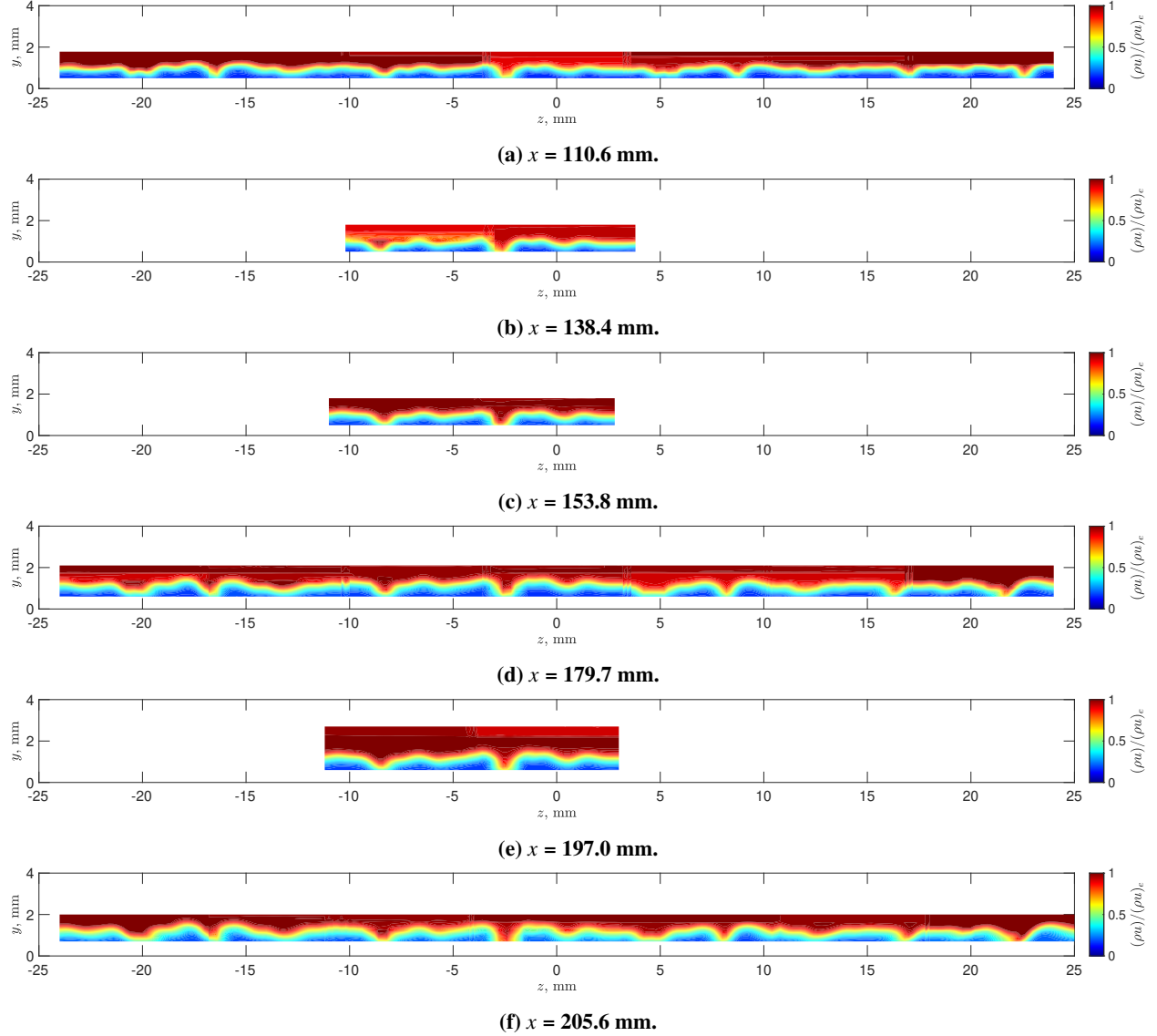


**Fig. 8 Mean mass flux contours in the wake of the pseudorandom roughness in quiet flow:  $M = 3.5$ ,  $Re = 12.6 \times 10^6/m$ .**

itself. However, this probe was aligned to the center of the back of the model several times over the testing period, so that large an offset in the spanwise position is not likely to be due to the alignment of the traverse.

At  $x = 205.6$  mm, there appear to be two disturbances very close to each other between  $z = -5$  and  $0$  mm in Fig. 10f. These look similar to odd mode and even mode instabilities that are distorted by the non-symmetric mean flow distortion shown in Fig. 8. A smaller-amplitude set of disturbances is noted at a location between  $z = -20$  and  $-15$  mm, which is repeated on the other half of the wake at  $z = +5$  and  $+10$  mm, albeit at an even smaller amplitude. The differences between the  $-z$  side of the plate and the  $+z$  side of the plate are primarily that the  $-z$  side has larger amplitude disturbances. The cause of this difference is unknown but could be due to a variety of factors such as edge and corner effects of the insert on the flow or nonuniformity of the incoming flow due to steps and gaps in the rotated insert. Since these inserts are machined for an initial fit in the model, the small steps and gaps produced by a  $180^\circ$  rotation of the insert may affect the seal around it, which could introduce these higher initial amplitudes.

The measurements of the roughness have a resolution of  $0.0148$  mm in each direction, yielding  $1727$  points across the streamwise direction of the pseudorandom roughness, but the dimensions of the insert are limited to only approximately  $50$  mm by  $25$  mm. Fast Fourier transforms (FFTs) of the measured surface roughness were made for the pseudorandom

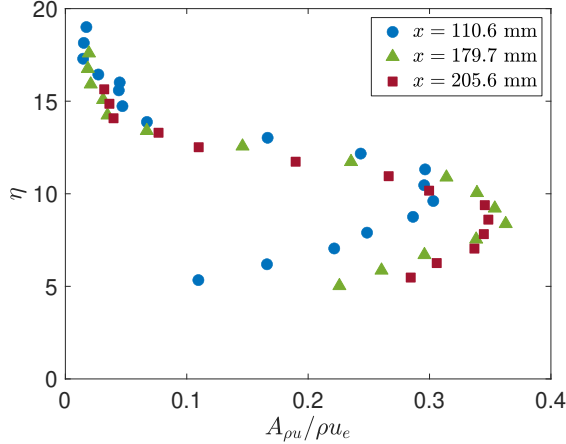


**Fig. 9** Streak strength profiles for  $x = 110.6$  mm,  $179.7$  mm, and  $205.6$  mm in the wake of the rotated pseudorandom roughness in quiet flow:  $M = 3.5$ ,  $Re = 12.6 \times 10^6/m$ .

roughness across 379 streamwise-oriented line measurements over a region between  $z = -5.2$  and  $0.4$  mm. These FFTs were then averaged together to form a wavelength spectra displayed in Fig. 11. While the overall spectral content of the pseudorandom roughness is fairly flat (black line in Fig. 11), it is possible that the section of the roughness just upstream of the observed instabilities has some type of dominant wavelength. Due to the dimensions of the roughness insert, the resolution of the wavelength spectra is incredibly coarse. However, a peak in the wavelength spectra near  $4$  mm and  $10$  mm is observed in the region directly upstream of these two instabilities, and additional peaks near  $2$  mm and  $3$  mm are observed in the region directly upstream of the instability centered near  $z = -3.8$  mm.

The power spectral density of the most amplified instability near  $z = -3.8$  mm is provided in Fig. 12a and the most-amplified instability near  $z = -1.4$  mm is provided in Fig. 12b. The RMS amplitude growth of the  $75$ -kHz instability (integrated over a  $5$  kHz bandwidth) is provided and compared to the maximum RMS of the full bandwidth across the entire span in Fig. 12d. At  $x = 110.6$  mm, the largest disturbance in the boundary layer near  $z = -3.8$  mm is a broad peak centered around  $74.2$  kHz. The instability near  $z = -1.4$  mm has a lower-amplitude broad peak centered around  $72.8$  kHz. Some low-frequency disturbances ( $f < 10^4$  Hz) are present in the mass-flux measurements.

A comparison of the instability growth for these disturbances is provided in Fig. 12c for four locations. As measurements continue farther downstream in the  $x$ -direction, the instabilities at both  $z = -3.8$  mm and  $z = -1.4$  mm grow larger until they saturate in amplitude near  $x = 179.7$  mm. At  $x = 197.0$  mm, the instability near  $z = -3.8$  mm starts to decrease in amplitude and some additional spectral broadening is evident between frequencies of  $26$  and  $57$  kHz, indicating the start of breakdown to turbulence. At  $x = 205.6$  mm, the peak frequency is nearly the same as at  $x = 197.0$  mm, but the amplitudes of the broadband frequencies increase further. For the instability centered near  $z = -1.4$  mm, the RMS amplitude of the instability also increases until  $x = 179.7$  mm. However, the amplitude remains relatively constant until the end of the measurement region at  $z = 205.6$  mm. The lower-frequency content of these measurements by the last measurement station has also increased to approximately the same amplitude as the instability near  $z = -3.8$  mm, as shown in Fig. 12c.

## VIII. Comparison to Previous Roughness Patch Measurements

The previous measurements of disturbances in the wake of the pseudorandom roughness indicated that the largest amplitude instability appeared to originate from the wake of the tallest roughness [9]. However, when the insert was rotated  $180^\circ$ , a different type of instability appears to be generated, and it does not appear to originate from the tallest roughness. The instability that appears to break down, centered at  $z = -3.8$  mm, will be the one referred to for the purposes of this comparison. An examination of the frequency content of these disturbances indicates that different instabilities appear to grow in the wake. Figure 13 compares the power spectra of the largest amplitude instability in the wake of the pseudorandom roughness for the original rotation (Rot1) and the current rotation of the roughness (Rot2) at select locations downstream of the leading edge of the flat plate. The largest amplitude instability that appears in Rot1 occurred in the range of  $z = -10$  to  $-6$  mm while the largest amplitude instability that appears in Rot2 occurred in the

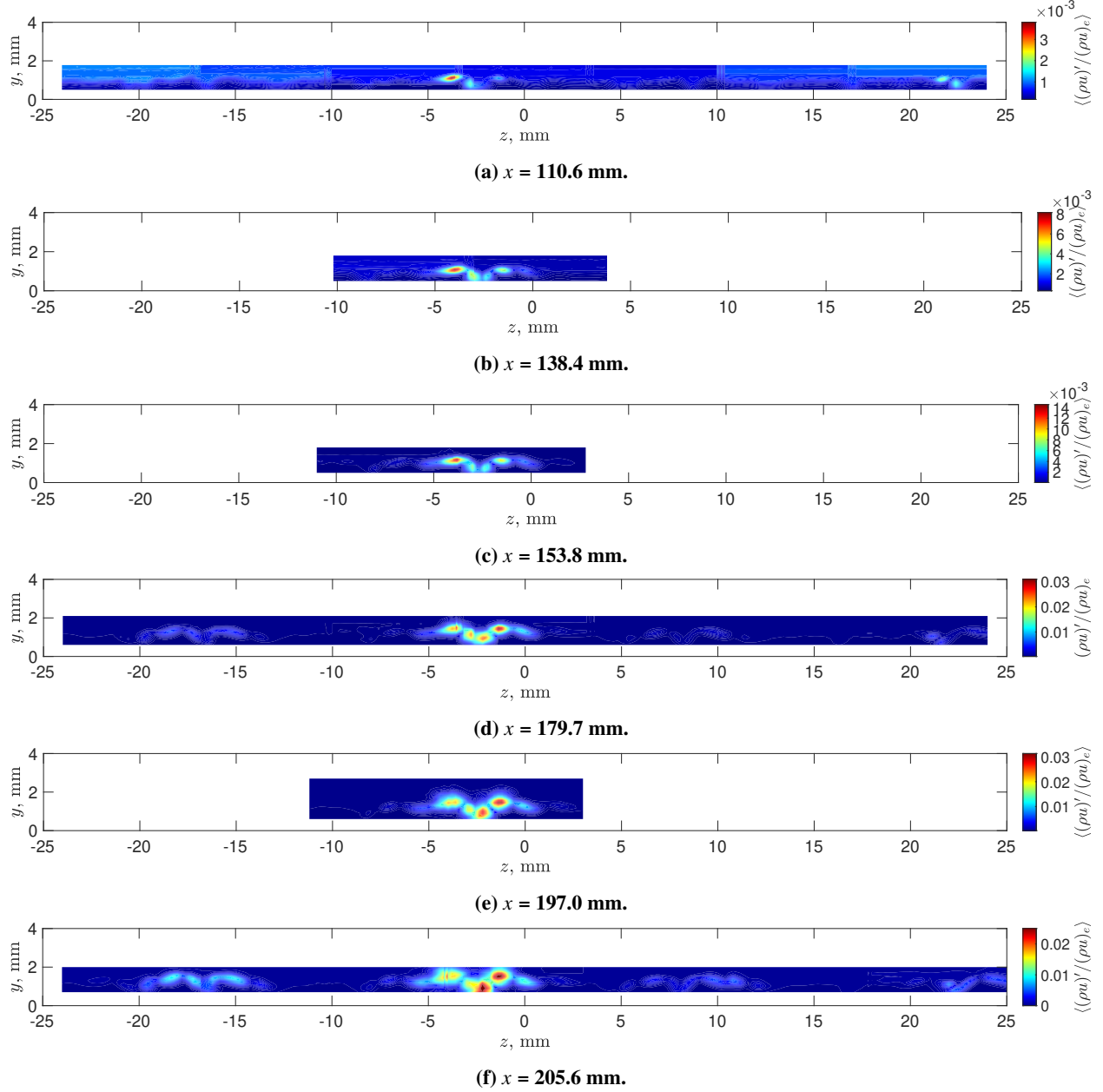


**Fig. 10** RMS mass-flux fluctuation contours of a 75 kHz instability in the wake of the rotated pseudorandom roughness in quiet flow:  $M = 3.5$ ,  $Re = 12.6 \times 10^6/m$ .

range of  $z = -6$  to  $-3$  mm.

At  $x = 110.6$  mm from the leading edge, the largest amplitude instability appears to be centered around 75 or 80 kHz, and is present in the wake for both Rot1 and Rot2. For Rot2, this instability reaches a much larger amplitude at this location than for Rot1. By  $x = 153.8$  mm, the amplitudes of the largest-amplitude instability are more comparable for the wakes of both rotations of the pseudorandom roughness. However, at  $x = 153.8$  mm, the 75-kHz instability is more amplified in the wake of Rot2, whereas a 100-kHz instability is more amplified in the wake of Rot1. This 75-kHz instability in wake of Rot2 also appears to have some higher peaks around 175 kHz, indicating the presence of some nonlinearity or other modes of disturbances. Autocorrelation of these measurements was not performed at this time, but may be done in future work. At farther downstream stations, this 75-kHz instability grows largest in the wake of Rot2, saturates at  $x = 179.7$  mm, and then decays by  $x = 205.6$  mm, indicating the early stages of transition to

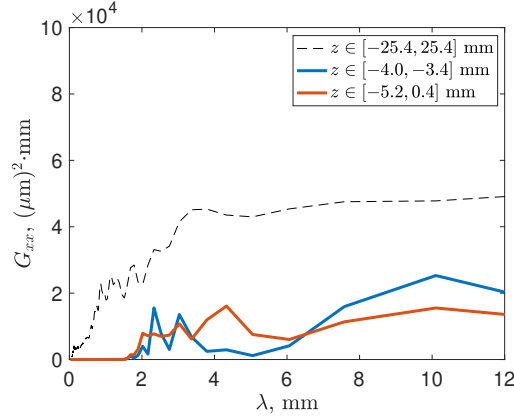


**Fig. 11** Wavelength spectra of pseudorandom roughness in the streamwise direction for the region upstream of the observed instabilities ( $z \in [-5.2, 0.4]$  mm and  $z \in [-4.0, -3.4]$  mm) compared to the overall roughness ( $z \in [-25.4, 25.4]$  mm.)

turbulence. On the other hand, the 100-kHz instability in the wake of Rot1 grows larger without decaying. For both configurations, Rot1 and Rot2, a 75-kHz and a 100-kHz instability appear in the wake of the pseudorandom roughness. However, the wake of Rot1 promotes the growth of the 100-kHz instability while the wake of Rot2 promotes the growth of the 75-kHz instability.

At the same distance from the leading edge, the mode shapes present in the wake are different. A comparison of the measured instability in the wake of the roughness is provided in Fig. 14. The instability in the wake of Rot1 appears to be a single mode in the wake of the tallest peaks of the pseudorandom roughness, centered at  $(z, x) = (-7.75, 48.13)$  mm and  $(z, x) = (17.25, 48.13)$  mm at 271- $\mu$ m tall. This instability mode for Rot1 has a shape similar to that of an even mode that is distorted, which is typically seen as a result of the non-symmetric flow around the irregular features in the roughness patch.

In comparison, the tallest peaks of Rot2 of the pseudorandom roughness are located at  $(z, x) = (7.75, 34.72)$  mm and  $(z, x) = (-17.25, 34.72)$  mm (Fig. 10). The instability observed in Rot2 looks more similar to a distorted odd mode, and the presence of a second instability closer to the centerline ( $z = 0$ ) of the wake may have an impact on the shape of this instability. The amplitude of the measured instabilities here are relatively small, so a better comparison of the wake of Rot2 to the wake of Rot1 may be made at  $x = 153.8$  mm, where the magnitude of the instabilities are similar.

Limited data were acquired across the span of the flat plate at  $x = 153.8$  mm for both Rot1 and Rot2 orientations of the pseudorandom roughness. These measurements were made at downstream locations where disturbances were expected to grow. Contour maps of the RMS mass flux fluctuations are provided in Fig. 15 for both Rot1 and Rot2. The center frequencies investigated, still using a 5-kHz bandwidth, include 80 kHz for Rot1, 75 kHz for Rot2, and 100 kHz for both rotations. The power spectra for the largest-amplitude instabilities at this  $x$ -station indicate that the 100-kHz instability should be the largest for Rot1 and the 75-kHz instability should be largest for Rot2. However, there is also a second peak in the power spectra near 80 kHz for Rot1.

The mode shapes are not centered downstream of the largest amplitude roughness, nor are they the same shape as when they were in Ref. [9], indicating different instabilities are present for Rot2 compared to Rot1. In fact, near the center of the roughness patch, Rot2 has two instabilities physically situated side by side that are centered around  $z = -1.7$  mm and  $-3.8$  mm while Rot1 has a single instability centered around  $z = -8.0$  mm. These disturbances are repeated near the outside edges of the flow field due to the repeated pattern in the pseudorandom roughness.

Figure 16 compares the RMS amplitude of the most-amplified disturbances in the wake of the egg crate roughness, Rot1 of the pseudorandom roughness, and Rot2 of the pseudorandom roughness at a freestream unit Reynolds number of  $12.6 \times 10^6/m$ . Rot2 of the pseudorandom roughness appears to transition earlier than both Rot1 of the pseudorandom roughness and the egg crate roughness. However, the amplitude of the disturbances at saturation is significantly lower than what was observed for both of these other roughness patterns.

The results of the egg crate roughness in Ref. [8] indicate that the roughness patch modifies the incoming first-mode disturbances and amplifies a particular instability to grow large and break down. In the case of the egg crate roughness, this was a 75-kHz AA instability (an antisymmetric or odd mode with the same wavelength of the roughness). Rot1

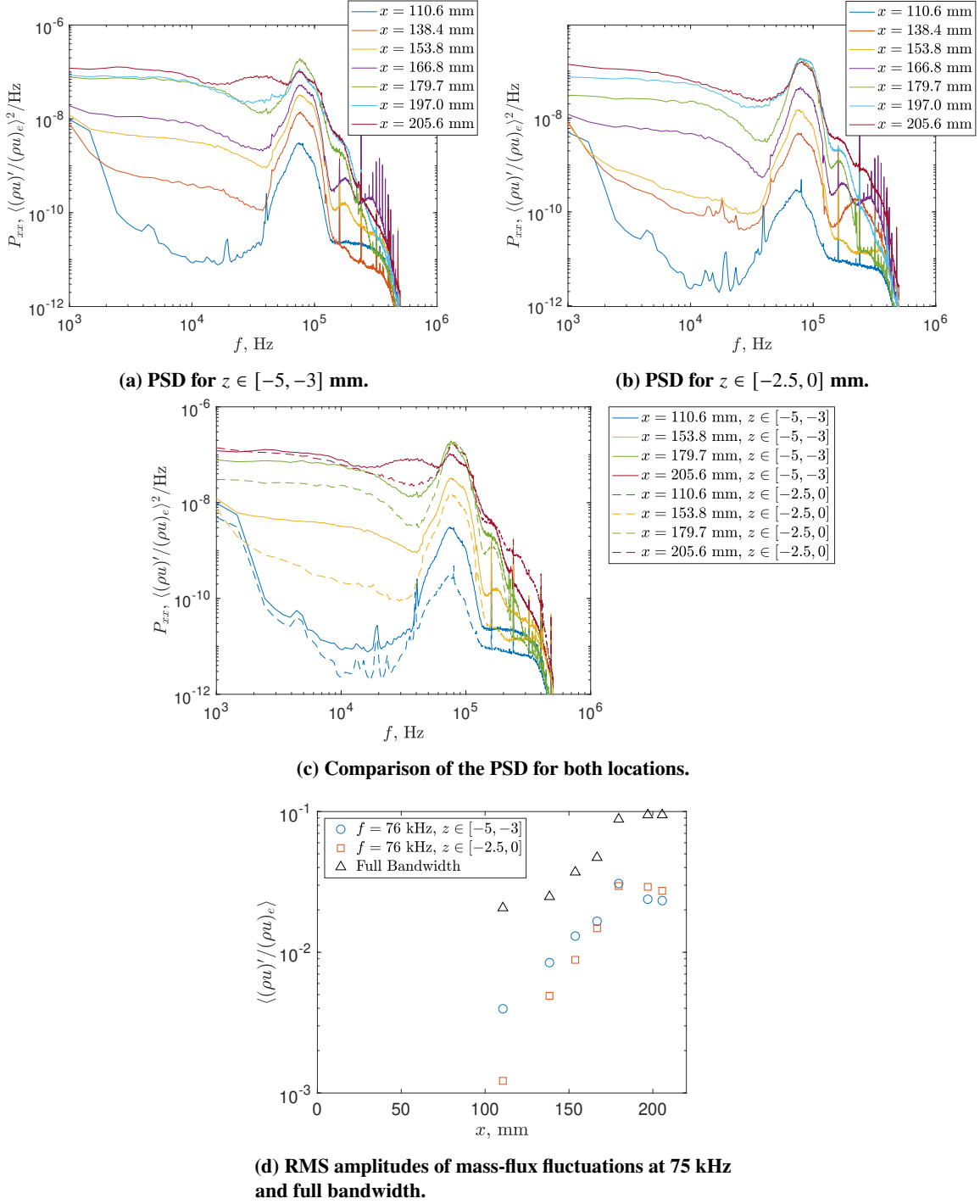


**Fig. 12 Growth of the largest-amplitude instability at two locations near the centerline.**

promotes the growth of a 100-kHz instability, which grows large and then saturates. This disturbance appears to be slower-growing, given the slope of the RMS amplitudes of the disturbance. Rot2 promotes the growth of a 75-kHz instability, which grows slower than the AA-mode in the wake of the egg crate roughness and saturates at a similar streamwise location to the egg crate roughness, albeit at a lower amplitude. Further theoretical and computational work may be required in order to understand why this particular instability grows large and transitions.

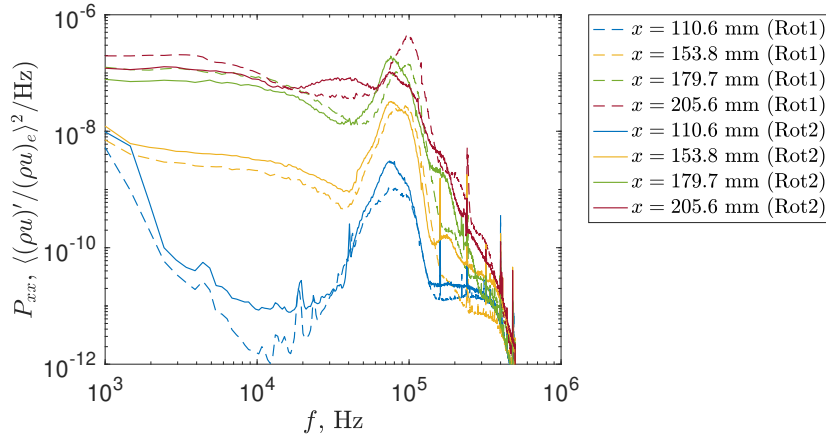


**Fig. 13** A comparison of the power spectra measured in the wake of a pseudorandom roughness. Original orientation (Rot1) is given by dashed lines and the current rotation (Rot2) is given by the solid lines.

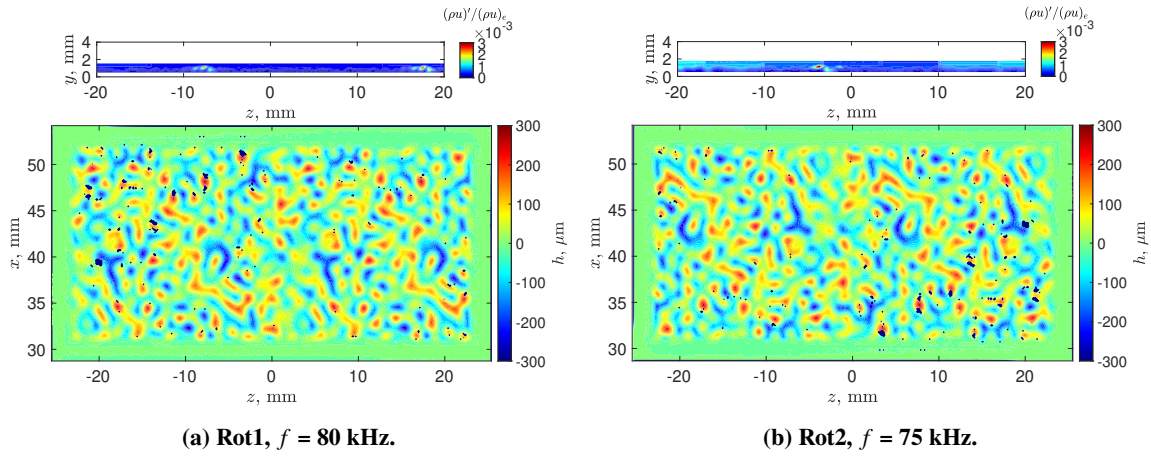


**Fig. 14** A comparison of RMS mass flux fluctuation measurements at  $x = 110.6$  mm downstream of the leading edge of the flat plate, relative to the position behind the pseudorandom roughness for both rotations:  $M = 3.5$ ,  $Re = 12.6 \times 10^6/m$ .

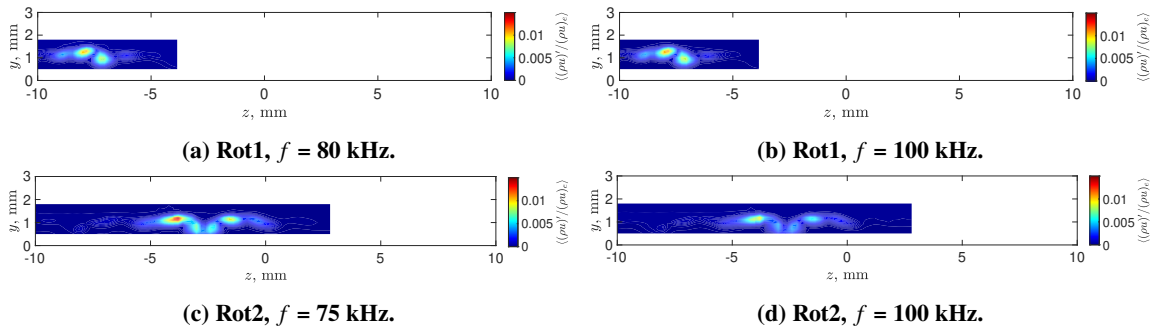


**Fig. 15** A comparison of measurements at  $x = 153.8$  mm downstream of the leading edge of the flat plate:  $M = 3.5$ ,  $Re = 12.6 \times 10^6/m$ .

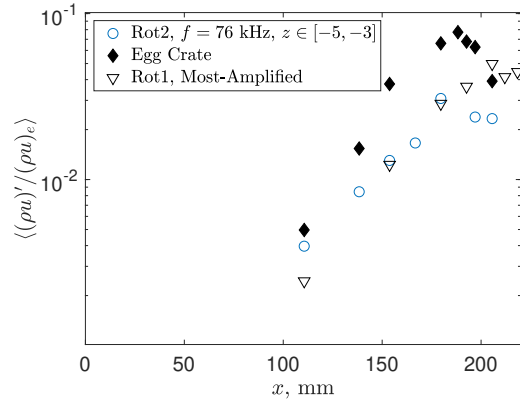


**Fig. 16 A comparison of RMS amplitudes of most-amplified disturbances for three different roughness configurations:  $M = 3.5$ ,  $Re = 12.6 \times 10^6/m$ .**

## IX. Summary

Measurements of the mean and fluctuating components of mass flux were made in the wake of a pseudorandom roughness defined by a two-dimensional series of sine waves. Previous studies of this pseudorandom roughness showed the growth of a disturbance directly downstream of the tallest roughness. Presently, a  $180^\circ$  rotation of the same roughness pattern produced a different set of instabilities that grew downstream. These instabilities were situated over a different portion of the roughness pattern and were centered around a different frequency than the previous rotation of the pseudorandom roughness. The cause of this change is still unknown.

Accurate prediction of transition location is important to reduce the uncertainty for the estimation of range and heat loads for high-speed vehicles. Several studies have been performed for simplified roughness, such as trip dots and strips, at both low and high speed. The investigation of pseudorandom roughness is a step toward understanding realistic roughness geometries, which is the ultimate goal of studies of distributed roughness. The next step for these types of investigations is to sample realistic roughness and model these surfaces as an analytic function or to force particular features on a background of smaller-scale random roughness, as was done previously in low-speed work at Texas A & M University. Ultimately, a better understanding of the physics that dominates transition due to distributed roughness will allow for better modeling of the transition process.

## References

- [1] Kegerise, M. A., Owens, L. R., and King, R. A., "High-Speed Boundary-Layer Transition Induced by an Isolated Roughness Element," *40th Fluid Dynamics Conference and Exhibit*, AIAA, 2010. <https://doi.org/10.2514/6.2010-4999>, AIAA Paper 2010-4999.
- [2] Kegerise, M. A., King, R. A., Choudhari, M., Li, F., and Norris, A., "An Experimental Study of Roughness-Induced Instabilities in a Supersonic Boundary Layer," *7th AIAA Theoretical Fluid Mechanics Conference*, AIAA, 2014. <https://doi.org/10.2514/6.2014-2501>, AIAA Paper 2014-2501.
- [3] Balakumar, P., and Kegerise, M. A., "Roughness-Induced Transition in a Supersonic Boundary Layer," *AIAA Journal*, Vol. 54, No. 8, 2016, pp. 2322–2337. <https://doi.org/10.2514/1.J054632>.
- [4] Chou, A., and Kegerise, M. A., "Transition Induced by a Streamwise Array of Roughnesses on a Supersonic Flat Plate," *47th AIAA Fluid Dynamics Conference*, AIAA, 2017. <https://doi.org/10.2514/6.2017-4515>, AIAA Paper 2017-4515.
- [5] Chou, A., King, R. A., and Kegerise, M. A., "Transition Induced by Tandem Rectangular Roughness Elements on a Supersonic Flat Plate," *2018 Fluid Dynamics Conference*, AIAA, 2018. <https://doi.org/10.2514/6.2018-3531>, AIAA Paper 2018-3531.
- [6] Chou, A., Kegerise, M. A., and King, R. A., "Transition induced by streamwise arrays of roughness elements on a flat plate in Mach 3.5 flow," *Journal of Fluid Mechanics*, Vol. 888, No. A21, 2020, pp. A21–1–A21–34. <https://doi.org/10.1017/jfm.2020.65>.
- [7] Chou, A., Kegerise, M. A., and King, R. A., "Transition Induced by an Egg-Crate Roughness on a Flat Plate in Supersonic Flow," *AIAA Aviation 2020 Forum*, AIAA, 2020. <https://doi.org/10.2514/6.2020-3045>.

- [8] Chou, A., Paredes, P., Kegerise, M. A., King, R. A., Choudhari, M., and Li, F., “Transition Induced by an Egg-Crate Roughness on a Flat Plate in Supersonic Flow,” *Journal of Fluid Mechanics*, Vol. 948, 2022), p. A27. <https://doi.org/10.1017/jfm.2022.510>.
- [9] Chou, A., Kegerise, M. A., and King, R. A., “Instabilities in the Wake of a Pseudorandom Roughness on a Supersonic Flat Plate,” *AIAA SCITECH 2023 Forum*, AIAA, 2023. <https://doi.org/10.2514/6.2023-0443>.
- [10] Downs, R. S., White, E. B., and Denissen, N. A., “Transient Growth and Transition Induced by Random Distributed Roughness,” *AIAA Journal*, Vol. 46, No. 2, 2008, pp. 451–462. <https://doi.org/10.2514/1.31696>.
- [11] Kuester, M. S., White, E. B., Sharma, A., Goldstein, D. B., and Brown, G., “Distributed Roughness Shielding in a Blasius Boundary Layer,” *44th AIAA Fluid Dynamics Conference*, 2014. <https://doi.org/10.2514/6.2014-2888>, AIAA Paper 2014-2888.
- [12] Sharma, A., Drews, S. D., Kuester, M., Goldstein, D. B., and White, E. B., “Evolution of disturbances due to discrete and distributed surface roughness in initially laminar boundary layers,” *52nd Aerospace Sciences Meeting*, AIAA, 2014. <https://doi.org/10.2514/6.2014-0235>, AIAA Paper 2014-0235.
- [13] Suryanarayanan, S., Goldstein, D. B., Brown, G. L., Berger, A. R., and White, E. B., “On the Mechanics and Control of Boundary Layer Transition Induced by Discrete Roughness Elements,” *55th AIAA Aerospace Sciences Meeting*, 2017. <https://doi.org/10.2514/6.2017-0307>, AIAA Paper 2017-307.
- [14] Suryanarayanan, S., Goldstein, D. B., Berger, A. R., White, E. B., and Brown, G. L., “Mechanisms of Roughness-Induced Boundary-Layer Transition Control by Shielding,” *AIAA Journal*, Vol. 58, No. 7, 2020, pp. 2951–2963. <https://doi.org/10.2514/1.J058950>.
- [15] Beckwith, I. E., Creel, Jr., T. R., Chen, F.-J., and Kendall, J. M., “Free stream noise and transition measurements in a Mach 3.5 pilot quiet tunnel,” *21st AIAA Aerospace Sciences Meeting*, AIAA, 1983. <https://doi.org/10.2514/6.1983-42>, AIAA Paper 1983-42.
- [16] Chen, F. J., Malik, M. R., and Beckwith, I. E., “Boundary-Layer Transition on a Cone and Flat Plate at Mach 3.5,” *AIAA Journal*, Vol. 27, No. 6, 1989, pp. 687–693. <https://doi.org/10.2514/3.10166>.
- [17] Fransson, J. H., Brandt, L., Talamelli, A., and Cossu, C., “Experimental and Theoretical Investigation of the Nonmodal Growth of Steady Streaks in a Flat Plate Boundary Layer,” *Physics of Fluids*, Vol. 16, No. 10, 2004, pp. 3627–3638. <https://doi.org/10.1063/1.1773493>.